Supporting Information

Experimental Section

Chemicals. All chemicals including trimesic acid ($C_6H_3(CO_2H)_3$, 98%), molybdenum pentachloride ($MoCl_5$, 99%), copper chloride dihydrate ($CuCl_2•2H_2O$, 99%), potassium hydroxide (KOH, 99%), sodium hydroxide (NaOH, 99%) potassium nitrate (KNO_3, 99%), potassium nitrate-^{15}N ($K^{15}NO_3$, 99%), potassium nitrite (KNO_2, 97%), sodium citrate tribasic dihydrate ($C_6H_5Na_3O_7•2H_2O$, 99%), sodium nitroferricyanide dihydrate ($C_5FeN_6Na_2O•2H_2O$, 99%), sulfanilamide ($C_6H_8N_2O_2S$, 99%), salicylic acid ($C_7H_6O_3$, 99%), N-(1-naphthyl) ethylenediamine dihydrochloride ($C_{12}H_{14}N_2•2HCl$, 98%), maleic acid ($C_{19}H_{17}ClFN_5S•C_4H_4O_4$, 98%), sodium hypochlorite solution (NaClO, 5% active chlorine basis) were purchased from Aladdin and used directly without further purification. Ethyl alcohol (C_2H_5OH, 99.7%) and phosphoric acid (H_3PO_4, 85%) were purchased from Sinopharm Chemical Reagent Co., Nafion 117 solution (~5% in a mixture of low aliphatic alcohols and water) was purchased from Sigma-Aldrich. Deionized water from Millipore Q water purification system was used to make the solutions.

Preparation of catalysts. The catalysts were synthesized by co-precipitation. $C_6H_3(CO_2H)_3$ (4 g) was dissolved in 80 mL of ethanol, $CuCl_2•2H_2O$ (2 g) was dissolved in 40 mL of deionized water, and $MoCl_5$ (0.8 g) was dissolved in 20 mL of ethanol (the molar ratio of Cu to Mo was 4:1). The three solutions were mixed under stirring, and after stirring for 8 hours, the mixture was centrifuged to obtain the precipitate, which was washed three times with a water-ethanol solution. The precipitate was dried in an oven at 70 °C for 24 hours, followed by grinding into fine powder. Subsequently, the fine powder mixture was subjected to calcination in an air atmosphere, with the temperature increasing from 25 °C to 600 °C at a heating rate of 3 °C/min, maintained at 600 °C for 2 hours. After cooling to room temperature, $Cu_3Mo_2O_9$/CuO was obtained. CuO was prepared using the same method without the addition of $MoCl_5$. $Cu_3Mo_2O_9$ was prepared using the same method except for adjusting the initial Cu/Mo feeding ratio.

Characterizations. The crystal structures of the as-prepared samples were examined by a Bruker D8 X-ray diffractometer (XRD) equipped with a Cu Kα radiation (λ = 1.5406 Å) source (40 kV, 40 mA).

Raman spectroscopy was performed on a microscopic laser confocal Raman spectrometer (Horiba LabRAM HR800). The morphology and microstructure were studied by field-emission scanning electron microscopy (FESEM, SU8600) and field-emission transmission electron microscopy (FETEM, JEM-F200) equipped with an energy dispersive X ray (EDX) spectroscopy detector. The chemical states and elemental composition of the samples were analyzed by X-ray photoelectron spectroscopy (XPS) on an ESCALAB 250 photoelectron spectrometer (Thermo Fisher Scientific) with a monochromatized Al Kα source (hν = 1486.58 eV). The measurements were conducted with a total energy resolution of 0.45 eV, a step size of 0.02 eV for all spectra, and binding energies were calibrated against the C 1s peak at 284.8 eV.

Electrochemical measurements. The electrochemical measurements were carried out in a customized H-type glass cell separated by a Nafion 117 membrane (Fuel Cell Store) at room temperature. A CHI 660D electrochemical workstation (Chenhua, Shanghai) was used to record the electrochemical response. The catalyst on carbon paper, saturated Hg/HgO electrode and platinum foil were used as the working, reference and counter electrode, respectively. All potentials reported in this work were calibrated to a reversible hydrogen electrode (RHE) according to $E_{RHE} = E_{Hg/HgO} + 0.098 + 0.059 \times pH$. The working electrode was prepared as follows: The catalyst ink was prepared by thoroughly mixing 5 mg of catalyst powder with 980 μL of an ethanol-deionized water mixed solution (volume ratio of 1:1) and 20 μL of Nafion solution (5 wt.%). The mixture was ultrasonicated for at least 12 h to form a homogeneous ink. Subsequently, the ink was uniformly coated onto a carbon paper (5 × 1 cm), achieving a catalyst loading of 1 mg/cm². For electrocatalytic NO_3^- reduction, a solution with 1 M KOH and 0.05 M KNO_3 was used as the electrolyte unless otherwise specified and was evenly distributed to the cathode and anode compartment. The electrolyte volume in the two parts of H-cell was 40 mL and was purged with high-purity Ar for 10 min before the measurement. The LSV curves were recorded at a scanning rate of 5 mV s^{-1}. The potentiostatic tests were conducted at constant potentials for 1 h at a stirring rate of 500 r.p.m. High-purity Ar was continuously fed into the cathodic compartment during the experiments. For consecutive cyclic tests, the potentiostatic measurements were performed at -0.5 V vs. RHE for 1 h at a stirring rate of 500 r.p.m. After electrolysis, the electrolyte was analyzed by UV-vis spectrophotometry as mentioned below. Then, the potentiostatic tests were carried out at the same conditions using the fresh electrolyte for the next cycle.

The YR of NH_3 was calculated using the following equation:

$$NH_3\ yield\ rate = \frac{(C_{NH3} * V)}{(t * m)} * 10^{-3} \quad (1)$$

The FE of NH_3 was estimated using the following equation:

$$FE_{(NH3)} = \frac{(8 * F * C_{NH3} * V * 10^{-6})}{(17 * Q)} * 100\% \quad (2)$$

where C_{NH3} is the measured NH_3 concentration (μg mL^{-1}); V is the volume of the electrolyte; t is the electrolysis time (1 h); m is the quality of the catalyst on the electrode; F is the Faraday's constant (96,485 C mol^{-1}); Q (C) is the total charge passed through the electrode, which is the integral of I-t curve.

Determination of ammonia-N. The amount of produced NH_3 was determined by the indophenol blue method using spectrophotometry. First, a certain amount of electrolyte after NO_3^-RR was extracted from the electrolytic cell and diluted to fall within the detection range. Subsequently, 2 mL of the diluted electrolyte was taken out and mixed with 2 mL of 1 M NaOH solution containing 5 wt.% salicylic acid and 5 wt.% sodium citrate, followed by adding 1 mL of 0.05 M NaClO and 0.2 mL of 1 wt.% $C_5FeN_6Na_2O$ (sodium nitroferricyanide) aqueous solution. After 2 h at room temperature, the UV-vis spectrophotometer was used to measure the absorption spectrum. As shown in Figure S4, a series of standard ammonium nitrate solutions were employed to make the concentration-absorbance calibration curve.

Determination of nitrite-N. The amount of produced NO_2^- was determined by Griess test. A mixture of N-(1-naphthyl) ethylenediamine dihydrochloride (0.2 g), p-aminobenzenesulfonamide (4 g), phosphoric acid (10 mL, ρ = 1.70 g/mL) and ultrapure water (50 mL) was used as the color reagent. After NO_3^-RR test, a certain amount of electrolyte was taken out from the electrolytic cell and diluted to 5 mL. Then, 0.1 mL color reagent was added into the aforementioned solution and mixed uniformly, and the absorption intensity at 540 nm was recorded after sitting for 20 min. The concentration-absorbance curve was calibrated using a series of standard potassium nitrite solutions as shown in Figure S7.

Determination of NH_3 using the ^1H NMR spectroscopy. 0.05 M $K^{15}NO_3$ or 0.05 M $K^{14}NO_3$ aqueous solution was used as the reactant for NO_3^-RR. After electroreduction, the electrolyte was taken out and the pH value was adjusted to weak acid using 5 M H_2SO_4. Then 1 mL of the electrolyte was taken out, followed by adding 100 μL of D_2O. Afterwards, the mixture was sent for ^1H NMR (600 MHz) analysis. The same procedure was applied to an electrolyte without KNO_3 for comparison. Additionally, maleic acid was used as an external standard to examine the ^1H NMR spectra recorded after different durations of electrolysis.

X-ray absorption spectroscopy characterization. X-ray absorption spectroscopy (XAS) was collected by employing synchrotron radiation light source at BL14W1 beamline of Shanghai Synchrotron Radiation Facility (SSRF) at room temperature. Energy calibration was performed with a Cu foil standard by shifting all spectra to a glitch in the incident intensity. Fluorescence spectra were recorded using a seven-element Ge solid state detector. The XAFS data were recorded in fluorescence excitation mode using a Lytle detector, and the spectra of all references were collected in the transmission mode. All samples were pelletized as disks of 13 mm diameter and 1 mm thickness using boron nitride as the binder. The acquired XAFS data were analyzed by Athena and Artemis software, according to the standard procedures. The k^2-weighted EXAFS spectra were obtained by subtracting the post-edge background from the overall absorption and then normalized with respect to the edge-jump step.

In-situ **ATR-SEIRAS.** The attenuated total reflectance surface-enhanced infrared absorption spectroscopy (ATR-SEIRAS) experiments were performed on a Nicolet iS50 FT-IR spectrometer equipped with a MCT detector cooled with liquid nitrogen and PIKE VeeMAX III variable angle ATR sampling accessory. The spectra were acquired at 0 V to -1.0 V vs. RHE. Each spectrum was acquired with a resolution of 2 cm^{-1} using a liquid Ar cooled mid-band mercury cadmium telluride (MCT) detector and averaged over 128 scans.

In-situ **Raman spectroscopy.** *In-situ* Raman spectroscopy measurements were conducted in a custom-designed three electrode SERS flow cell with a saturated Hg/HgO electrode as the reference electrode and a graphite rod as the counter electrode in the anode chamber. During the measurements, the electrolyte was circulated across the cell using a peristaltic pump. The Raman measurements were

performed on a LabRAM HR Evolution microscope (Horiba Jobin Yvon) with a 532 nm or 633 nm laser, a 50× objective, a monochromator (600 grooves/mm grating), and a CCD detector.

Density functional theory (DFT) calculations. Five-layer $Cu_3Mo_2O_9$ in (002) orientation was employed as the substrate to support the four-layer Cu atoms in (111) orientation. We carried out all spin-unrestricted DFT calculations in the Vienna ab initio simulation (VASP5.4.4) package. The exchange-correlation was simulated with PBE functional and the ion-electron interactions were described by the PAW method. The vdWs interaction was included using the empirical DFT-D3 method. For the construction of $Cu_3Mo_2O_9$(002)/Cu(111) slabs, vacuum thickness along the z-direction was set to be 25 Å; k-point sampling was set as 3 × 3 × 1 for the geometry optimization and 5 × 5 × 1 for the computation of electronic structure for all periodic structure with the cutoff energy of 450 eV; and dispersion correction, solvation treatment, dipole corrections, and convergence criteria were set as 0.02 $eV \cdot A^{-1}$ and 10^{-5} eV for force and energy, respectively. A 25 Å vacuum layer along the z direction was applied to avoid interlayer interference, and the three bottom layers of the substrates were fixed to decrease the computation consumption. It should be noted that the DFT simulations were conducted within a static periodic-slab model under implicit solvation and fixed-charge boundary conditions to approximate interfacial energetics. These calculations aim to capture qualitative interfacial trends rather than reproduce explicit dynamic, electrolyte, or constant-potential effects. Therefore, the mechanistic insights obtained should be interpreted as representative trends consistent with experimental observations rather than quantitative potential-dependent dynamics. The Gibbs free energy of reactant, intermediates, and product were obtained by calculating their phonon density of states, as depicted in Eq. 1:

$$G = E + ZPE + kT \int F(\omega) \ln[1 - \exp(-\frac{h\omega}{kT})] d\omega \quad (3)$$

where E is the energy, ZPE is the zero-point energy, the term $kT \int F(\omega) \ln[1 - \exp(-\frac{h\omega}{kT})] d\omega$ is the correction of Gibbs free energy via thermodynamic analysis.

Assembly of the Zn-NO_3^- battery. The Zn-NO_3^- battery measurements were carried out in a customized H-type glass cell which contains 40 mL cathode electrolyte (1 M NaOH + 0.05 M NO_3^-) and 40 mL anode electrolyte (1 M NaOH) separated by a Nafion 117 membrane (Fuel Cell Store) at room temperature. A CHI 660D electrochemical workstation (Chenhua, Shanghai) was used to record

the electrochemical response. The $Cu_3Mo_2O_9$/Cu and Zn plate were employed as the cathode and anode for Zn-NO_3^- battery, respectively. The electrolyte volume in the two parts of H-cell was purged with high-purity Ar for 10 min before the measurement. The LSV curves were recorded at a scanning rate of 5 mV s^{-1}. The galvanostatic tests were conducted at constant potentials for 1 h at a stirring rate of 500 r.p.m. High-purity Ar was continuously fed into the cathodic compartment during the experiments. After electrolysis, the electrolyte was analyzed by UV-vis spectrophotometry. The power density (P) of Zn-NO_3^- battery was determined by P = I × V, where I and V are the discharge current density and voltage, respectively. The electrochemical reactions in Zn-NO_3^- battery were presented as the following:

Cathode reaction: $NO_3^- + 7H_2O + 8e^- \rightarrow NH_4OH + 9OH^-$ (4)

Anode reaction: $4Zn + 8OH^- \rightarrow 4ZnO + 4H_2O + 8e^-$ (5)

Overall reaction: $4Zn + NO_3^- + 3H_2O \rightarrow 4ZnO + NH_4OH + OH^-$ (6)

Calculation of electrode potential for half reaction of cathode and anode. Since cathode and anode of Zn-NO_3^- were separated by a Nafion 117 membrane, the electrode potentials should be calculated individually:

$$E_{\text{anode}} = -\frac{1}{nF}(\Delta G_{\text{ano}} + RT \ln \frac{1}{[OH^-]^2}) \quad (7)$$

$$E_{\text{catode}} = -\frac{1}{nF}(\Delta G_{\text{cat}} + RT \ln \frac{[OH^-]^9[NH_4OH]}{[NO_3^-]}) \quad (8)$$

where n, F, ΔG, R, and T are electron transfer number, the Faraday's constant (96485 C/mol), standard molar Gibbs free energy change of chemical reaction at 298 K, gas constant (8.314 J/ (mol K)), and reaction temperature (298 K), respectively.

In the electrolyte system of 1 M NaOH and 1 M NaOH + 0.05 M NO_3^-. Assuming [NH_4OH] is 10^{-2} mol/L in cathode cell.

$$E_{\text{anode}} = -\frac{1}{nF}(\Delta G_{\text{ano}} + RT \ln \frac{1}{[OH^-]^2}) = -1.25$$

$$E_{\text{catode}} = -\frac{1}{nF}(\Delta G_{\text{cat}} + RT \ln \frac{[OH^-]^9[NH_4OH]}{[NO_3^-]}) = -0.12$$

$$E_{\text{overall}} = E_{\text{catode}} - E_{\text{anode}} = 1.13$$

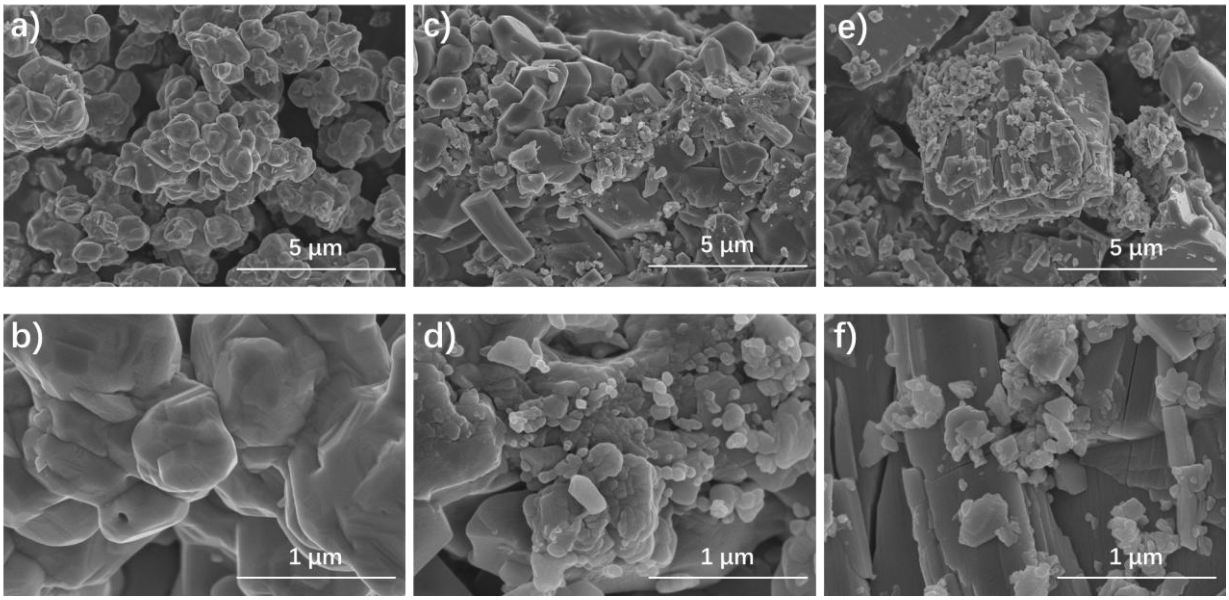

Fig. S1. SEM images of a-b) CuO, c-d) $Cu_3Mo_2O_9$/CuO, and e-f) $Cu_3Mo_2O_9$.

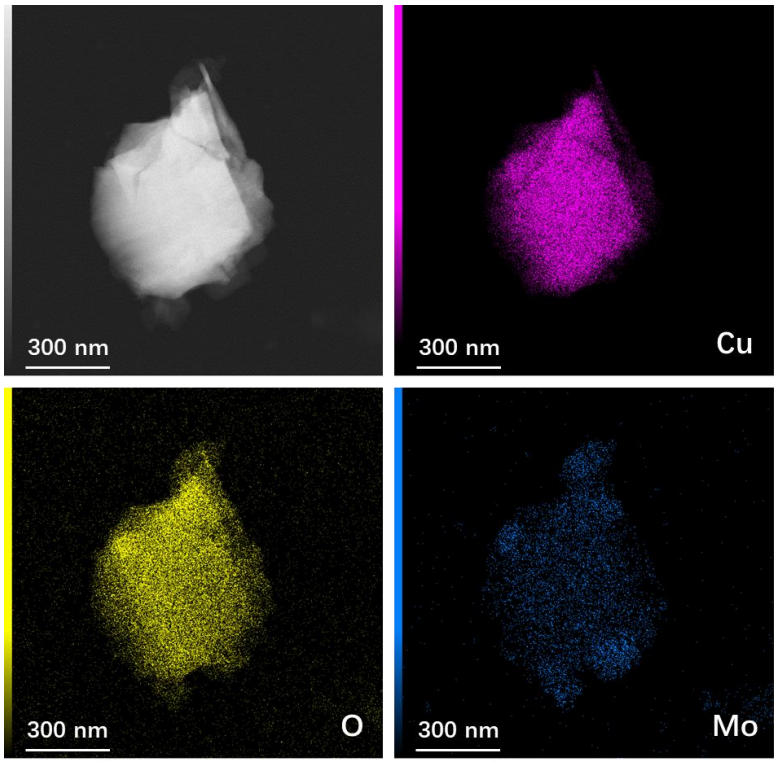

Fig. S2. STEM image and the corresponding EDX elemental mappings of $Cu_3Mo_2O_9$/CuO.

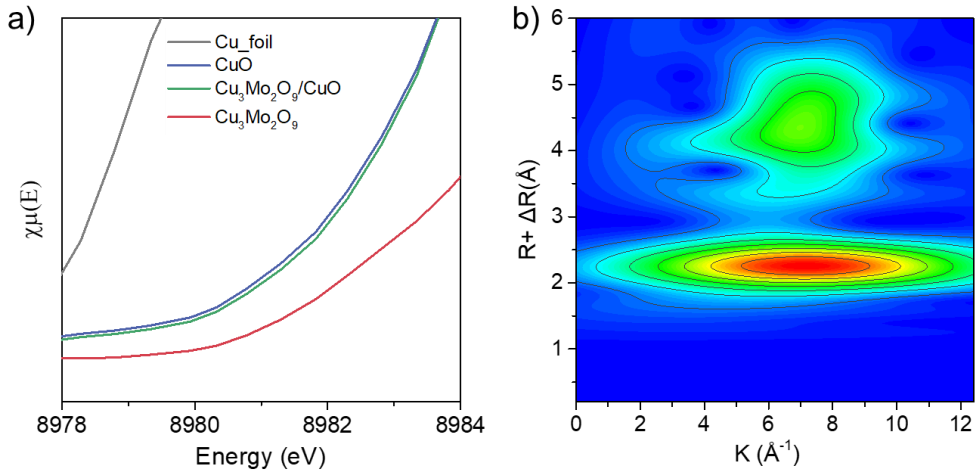

Fig. S3. a) Magnified normalized XANES spectra at the Cu K-edge. b) WT-EXAFS contour plots of Cu foil.

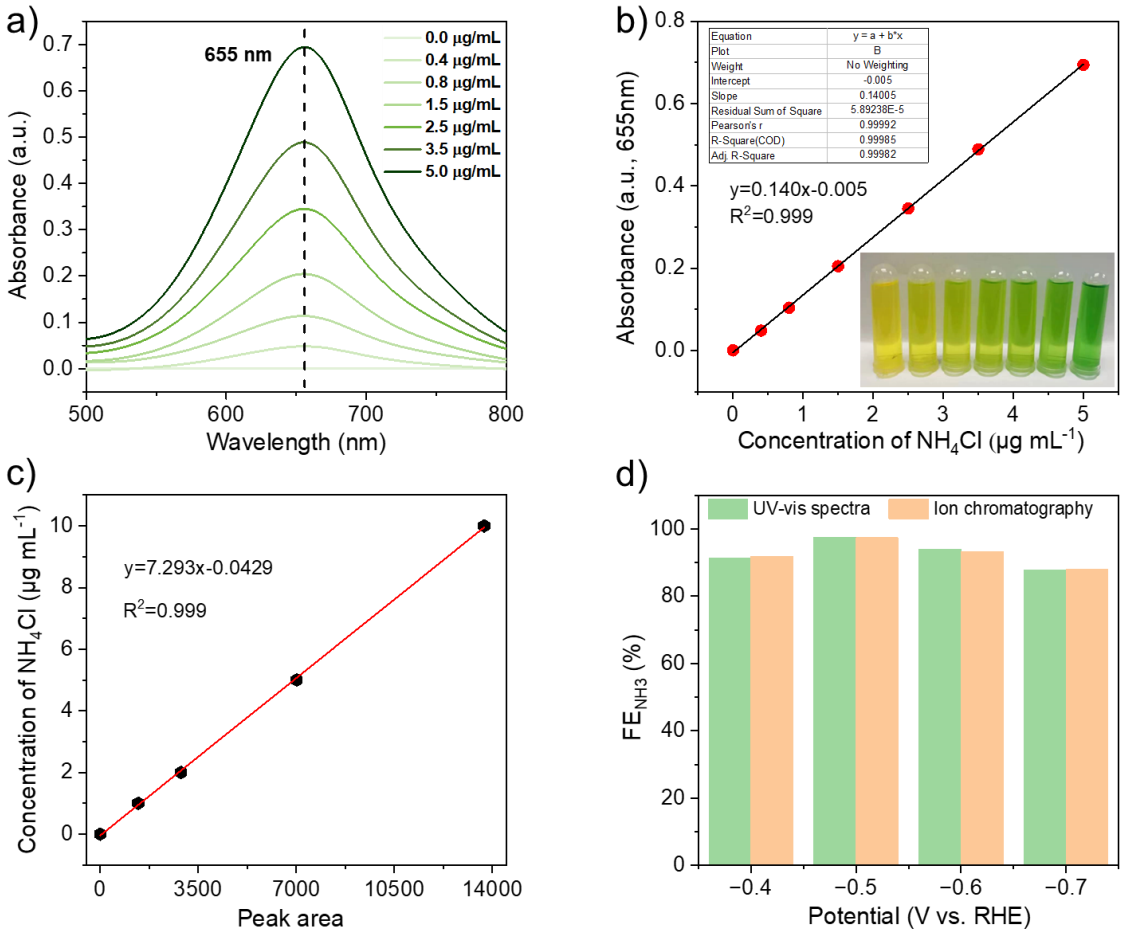

Fig. S4. UV-vis calibration curve of NH_3 in 1 M KOH using ammonium chloride solutions of known concentrations as standards. a) UV-vis curves of indophenol assays with NH_4^- ions after incubated for 2 h and b) calibration curve used for estimation of NH_3. c) Ion chromatography calibration curve of NH_3. d) NH_3 Faradaic efficiency (FE) over $Cu_3Mo_2O_9$/CuO at different applied potentials.

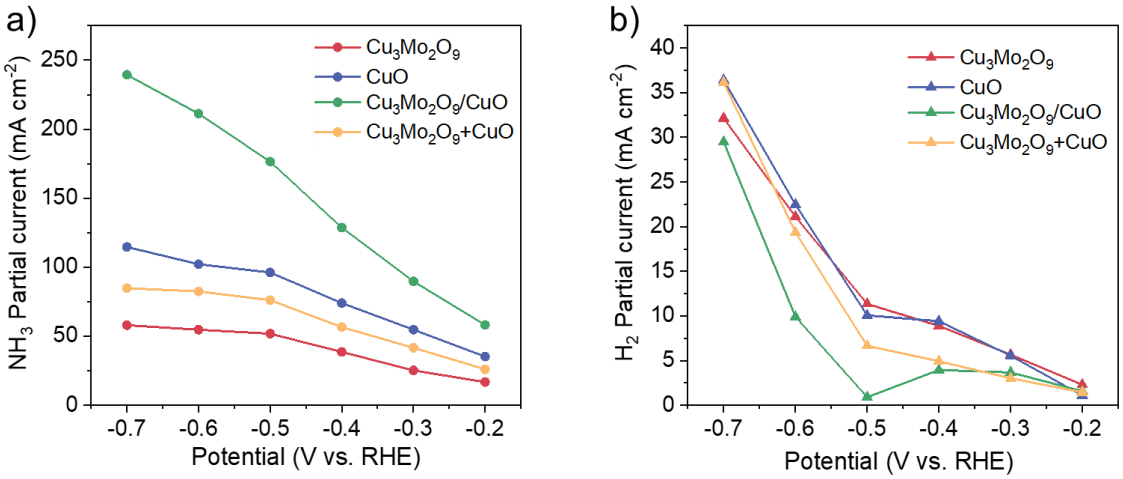

Fig. S5. The partial current densities of a) NH_3 and b) H_2 recorded over $Cu_3Mo_2O_9$, CuO, $Cu_3Mo_2O_9$/CuO and $Cu_3Mo_2O_9$ + CuO catalysts.

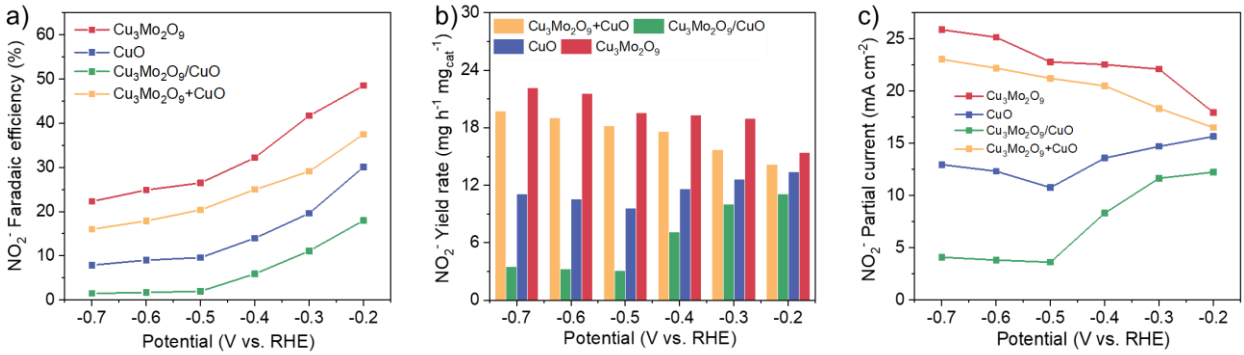

Fig. S6. a) FE, b) YR and c) partial current densities of NO_2^- at different cathodic potentials recorded over $Cu_3Mo_2O_9$, CuO, $Cu_3Mo_2O_9$/CuO, and $Cu_3Mo_2O_9$ + CuO catalysts.

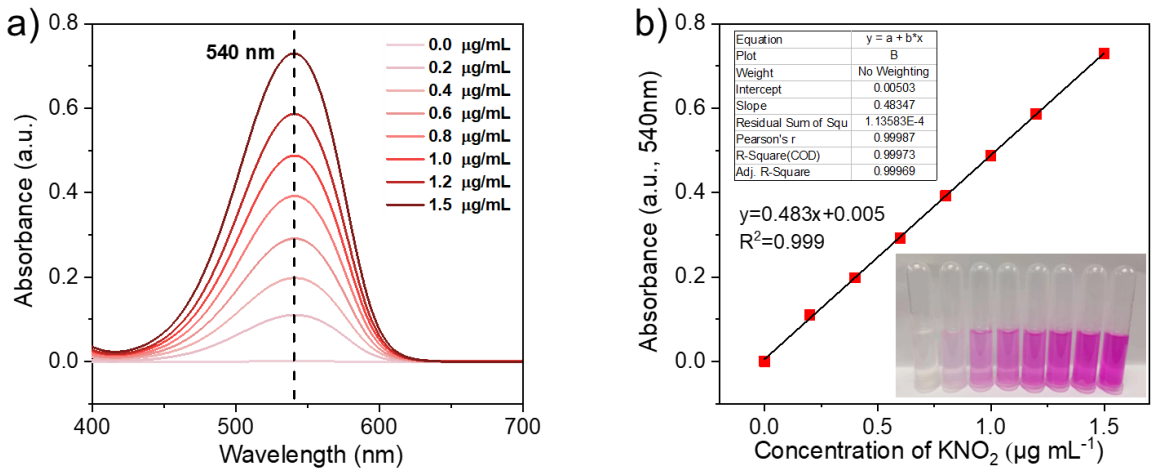

Fig. S7. UV-vis calibration curve of NO_2^- in 1 M KOH using KNO_2 solutions of known concentrations as standards. a) UV-vis curves of NO_2^- ions after sitting for 20 min and b) calibration curve used for estimation of NO_2^-.

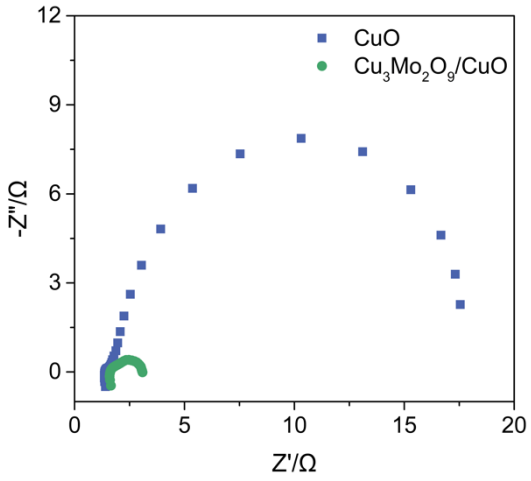

Fig. S8. Nyquist plots of CuO and $Cu_3Mo_2O_9$/CuO at -0.5V vs. RHE.

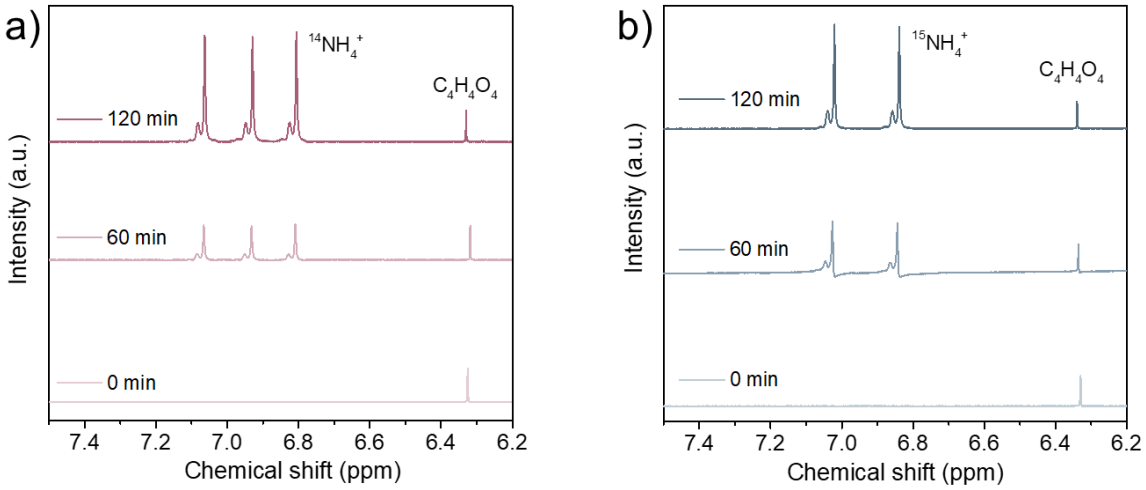

Fig. S9. ^{1}H NMR spectra of electrolytes after different durations of a) $^{14}NO_3^-$ and b) $^{15}NO_3^-$ reduction tests at -0.5 V vs. RHE.

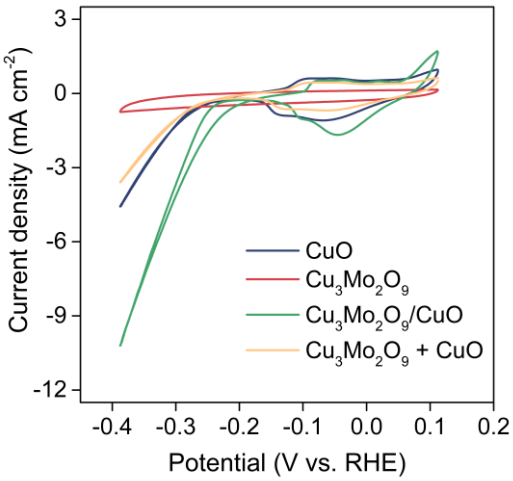

Fig. S10. CV curves of $Cu_3Mo_2O_9$/CuO, CuO, $Cu_3Mo_2O_9$ and $Cu_3Mo_2O_9$ + CuO recorded in 1 M KOH solution.

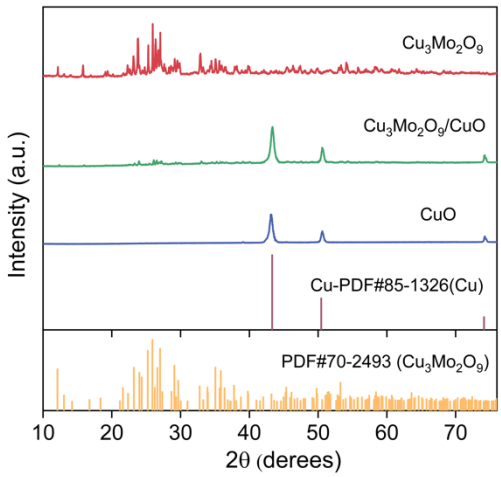

Fig. S11. XRD patterns of $Cu_3Mo_2O_9$, $Cu_3Mo_2O_9$/CuO and CuO after NO_3^-RR.

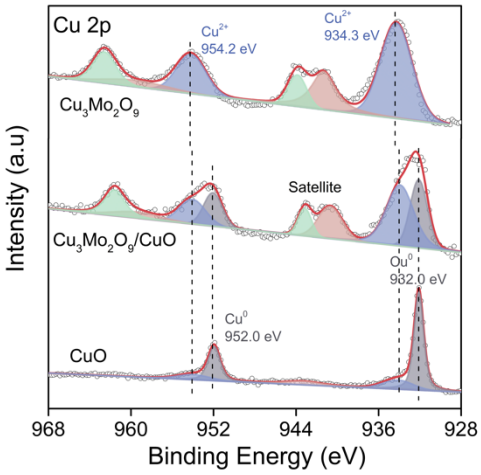

Fig. S12. High-resolution Cu 2p XPS spectra of $Cu_3Mo_2O_9$, CuO and $Cu_3Mo_2O_9$/CuO after NO_3^-RR.

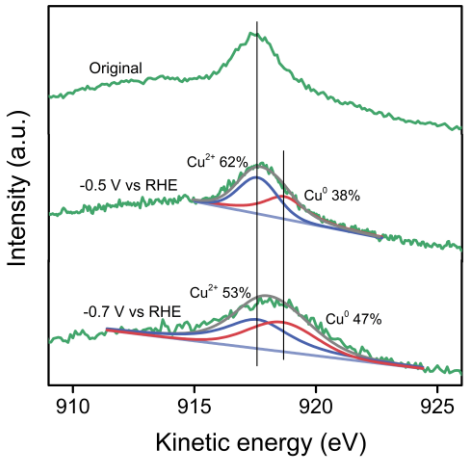

Fig. S13. The Cu auger electron spectroscopy spectra of original $Cu_3Mo_2O_9$/CuO, post-reaction $Cu_3Mo_2O_9$/CuO (-0.5 V vs. RHE) and post-reaction $Cu_3Mo_2O_9$/CuO (-0.7 V vs. RHE).

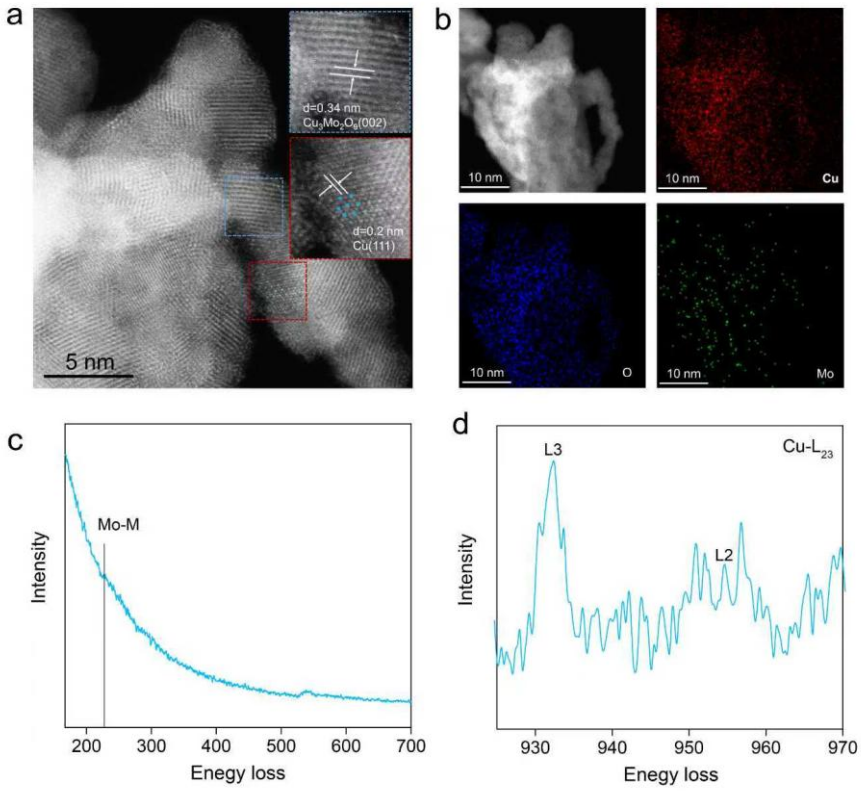

Fig. S14. (a) STEM image and (b) EDX mapping of $Cu_3Mo_2O_9$/Cu after NO_3^-RR. EEL spectra of the (c) Mo-M and (d) Cu-L_{23} of $Cu_3Mo_2O_9$/Cu after NO_3^-RR.

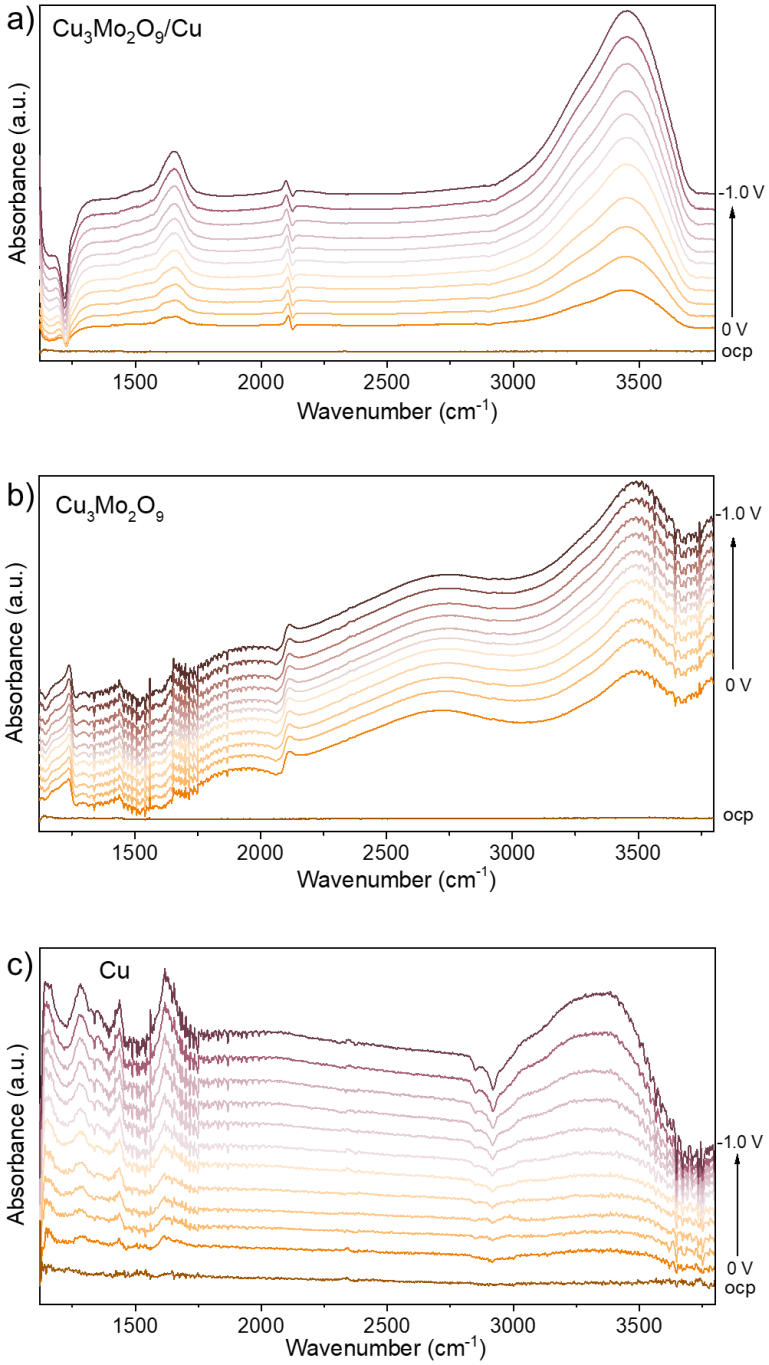

Fig. S15. *In-situ* ATR-SEIRAS spectra recorded in the potential window from 0 to -1.0 V vs. RHE over a) $Cu_3Mo_2O_9$/Cu, b) $Cu_3Mo_2O_9$ and c) Cu. The background spectrum was collected at OCP.

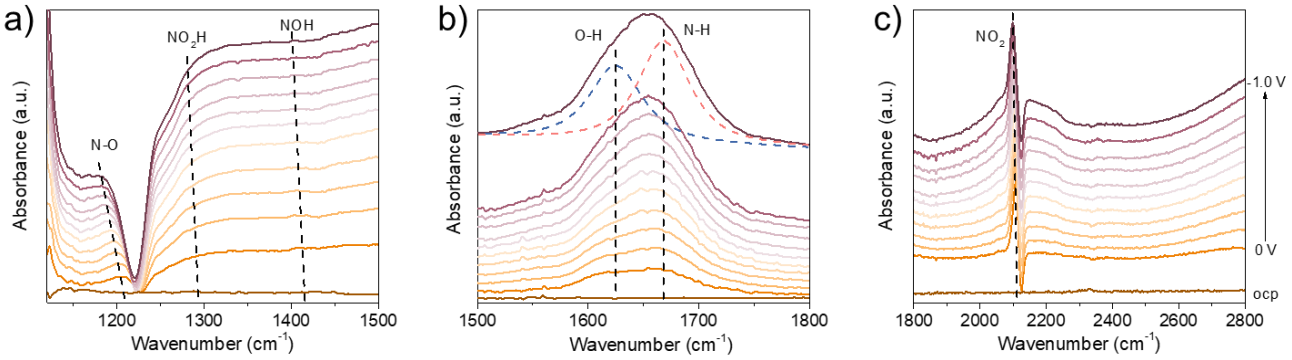

Fig. S16. *In-situ* ATR-SEIRAS spectra of $Cu_3Mo_2O_9$/Cu recorded in KNO_3 + KOH electrolyte at different applied cathodic potentials. The background spectrum was collected at OCP.

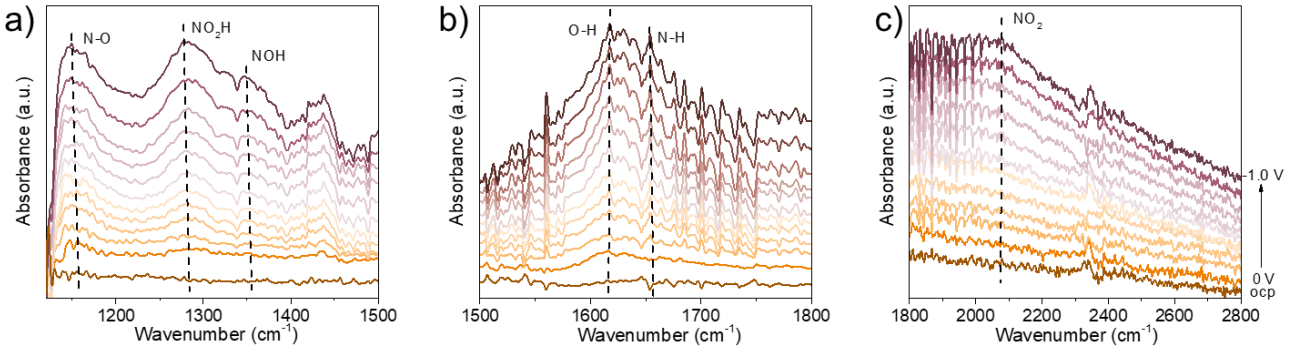

Fig. S17. *In-situ* ATR-SEIRAS spectra of Cu recorded in KNO_3 + KOH electrolyte at different applied cathodic potentials. The background spectrum was collected at OCP.

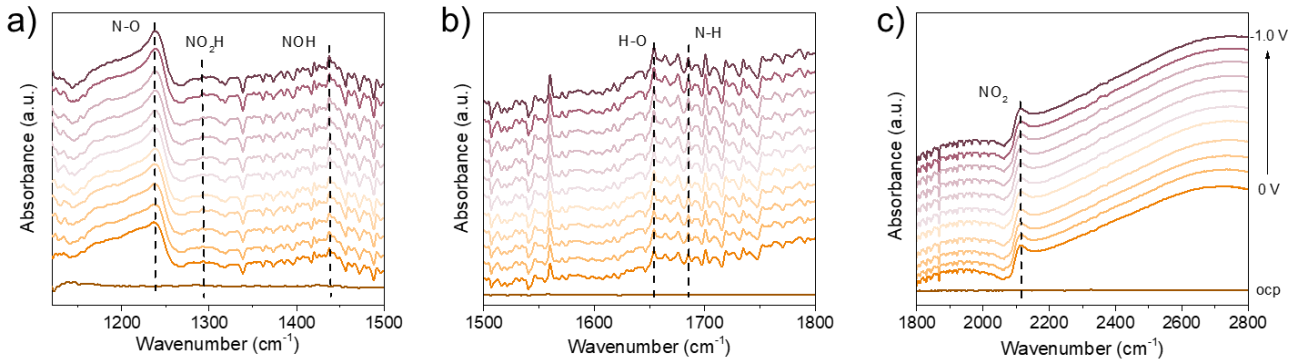

Fig. S18. *In-situ* ATR-SEIRAS spectra of $Cu_3Mo_2O_9$ recorded in KNO_3 + KOH electrolyte at different applied cathodic potentials. The background spectrum was collected at OCP.

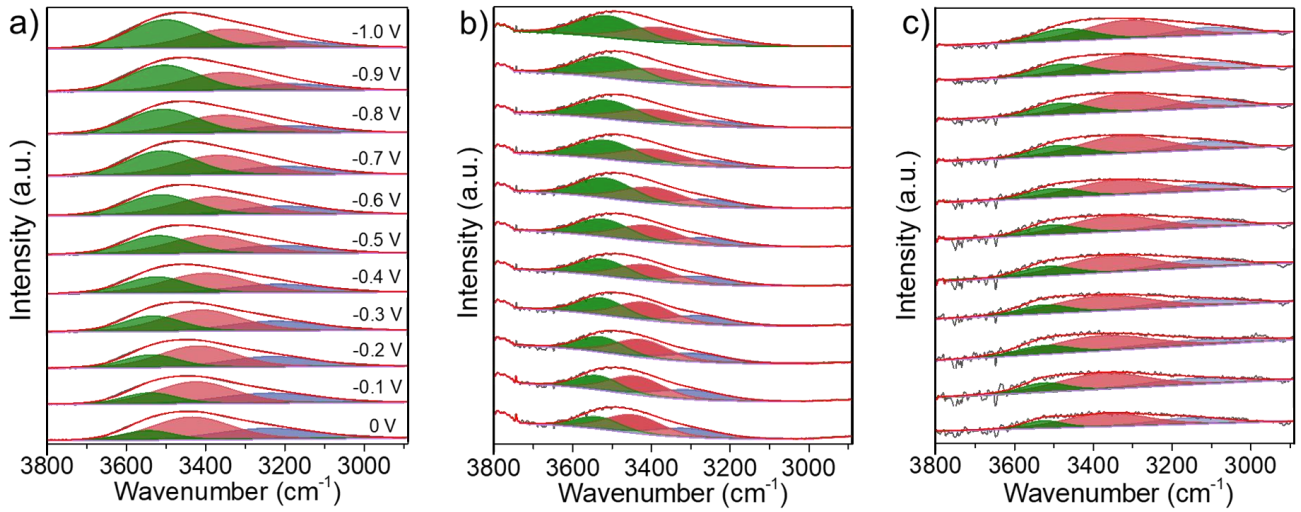

Fig. S19. *In-situ* ATR-SEIRAS measurements. Gaussian fit of three O-H stretching modes over a) $Cu_3Mo_2O_9$/Cu, b) $Cu_3Mo_2O_9$ and c) Cu.

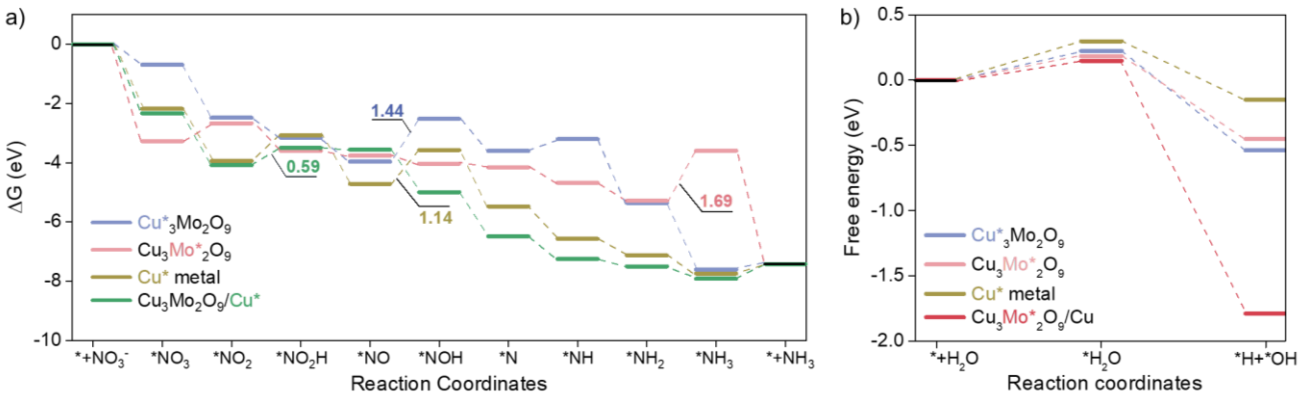

Fig. S20. a) Reaction free energies of NO_3^-RR on $Cu_3Mo_2O_9$/Cu*, $Cu^*_3Mo_2O_9$, $Cu_3Mo^*_2O_9$ and Cu* metal (the NO_3^- adsorption sites are highlighted using color coding and asterisk "*" label, and Cu* metal is based on Cu*(111) model). b) H_2O dissociation free energies on $Cu_3Mo^*_2O_9$/Cu, $Cu^*_3Mo_2O_9$, $Cu_3Mo^*_2O_9$ and Cu* metal (the H_2O adsorption sites are highlighted using color coding and asterisk "*" label).

Guided by post-reaction XRD, we built the interface as $Cu_3Mo_2O_9(002)/Cu(111)$ and computed all key energetics (**Fig. S21**). The qualitative bifunction remains: Cu sites favor $*NO_3^-$ deoxygenation steps, while Mo-O favors H_2O dissociation, and Cu(111) exhibits faster NO_3^-RR kinetics than Cu(100).

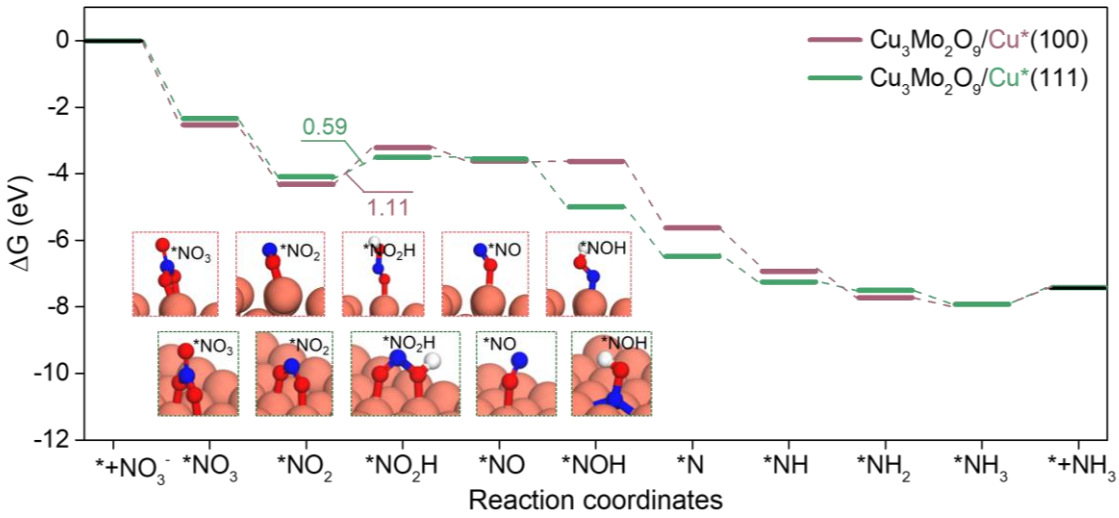

Fig. S21. Reaction free energies of NO_3^-RR on $Cu_3Mo_2O_9/Cu^*(100)$ and $Cu_3Mo_2O_9/Cu^*(111)$.

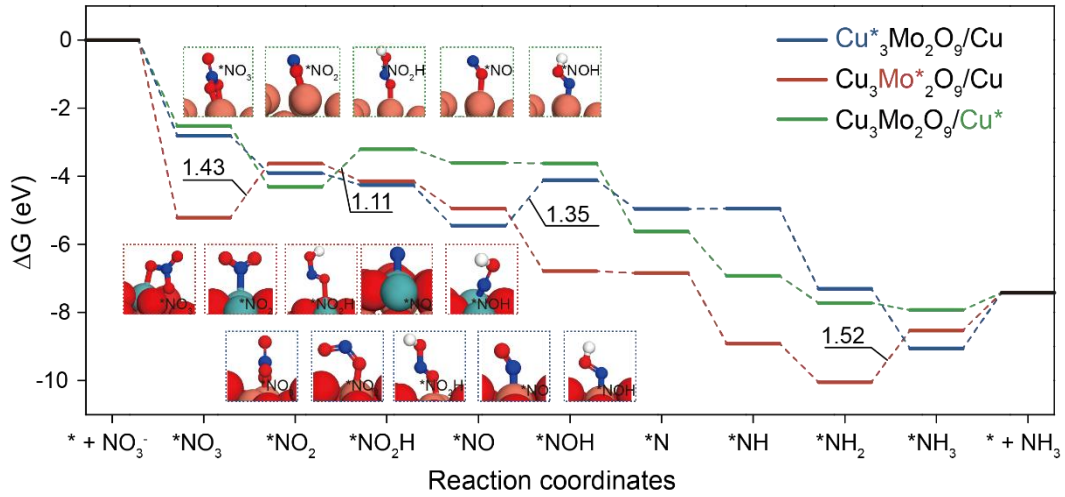

Fig. S22. Reaction free energies of NO_3^-RR on $Cu^*_3Mo_2O_9$, $Cu_3Mo^*_2O_9$ and Cu* metal (the NO_3^- adsorption sites are highlighted using color coding and asterisk "*" label, and Cu* metal is based on Cu*(100) model).

We have carried out systematic convergence tests with 2-, 3-, and 4-layer Cu (111) slabs (**Fig. S23**). The results show that the activation barrier for $*NO_2 \rightarrow *NO_2H$ decreases further with increasing slab thickness, and that the 4-layer slab provides more stable energetics. Accordingly, we have now adopted the 4-layer Cu (111) slab as our standard model. This ensures that the reported energetics are well-converged and physically reliable.

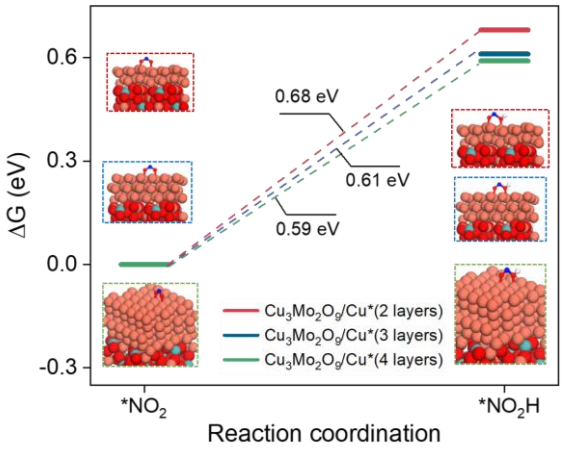

Fig. S23. ΔG of $*NO_2 \rightarrow *NO_2H$ on $Cu_3Mo_2O_9$/Cu*(111 2 layers), $Cu_3Mo_2O_9$/Cu*(111 3 layers) and $Cu_3Mo_2O_9$/Cu*(111 4 layers).

We built and relaxed the $Cu_3Mo_2O_9$ (002)/Cu (111) heterojunction using DFT optimization. The optimized structure shows a formation energy of -5.6 eV for $Cu_3Mo_2O_9$/Cu, indicating thermodynamic stability (**Fig. S24**). We also computed the electronic local function (**Fig. S25**), which revealed significant charge redistribution across the interface. This ensures that the heterojunction is physically meaningful and supports the electronic coupling in our mechanistic discussion.

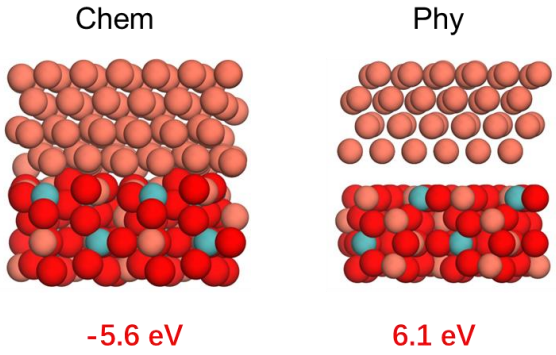

Fig. S24. Formation energy of $Cu_3Mo_2O_9$/Cu and physically mixed $Cu_3Mo_2O_9$ and Cu ($Cu_3Mo_2O_9$ + Cu).

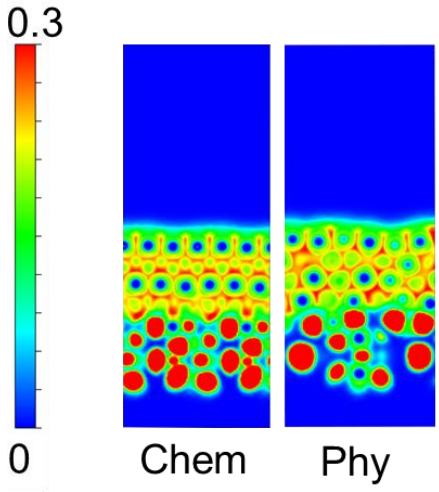

Fig. S25. Electronic local function of $Cu_3Mo_2O_9$/Cu and physically mixed $Cu_3Mo_2O_9$ and Cu ($Cu_3Mo_2O_9$ + Cu). The high ELF value regions (in red) indicate covalent bonds and lone pairs of electrons, while the low value regions (in blue) indicate electron delocalization.

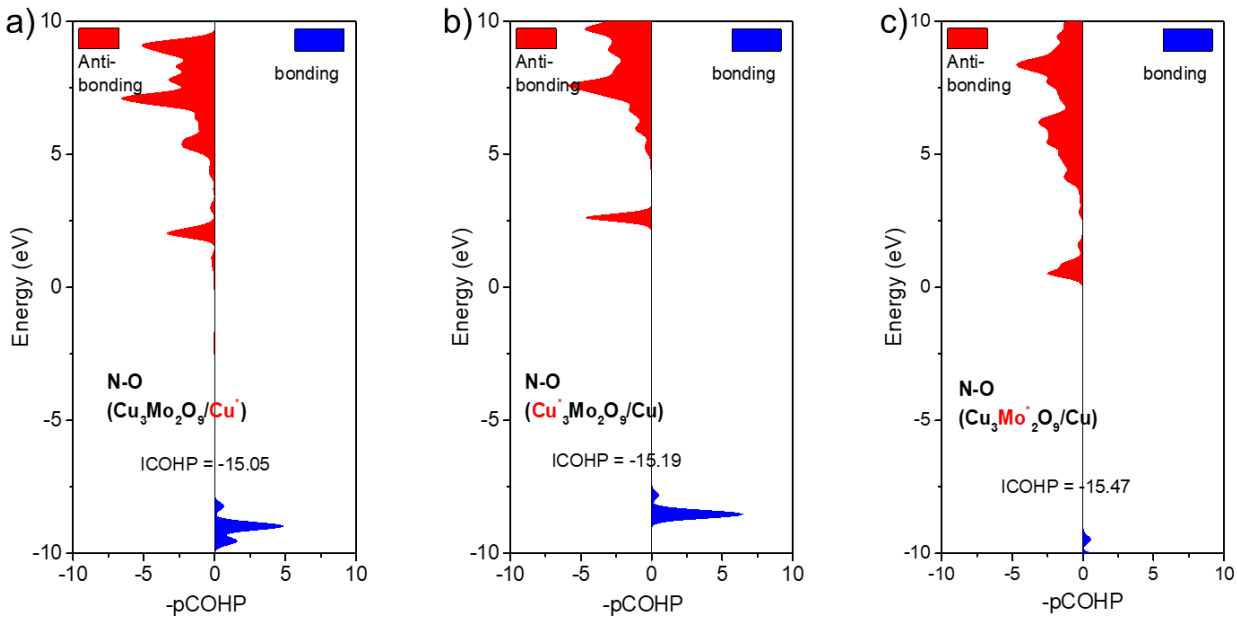

Fig. S26. Projected crystal orbital Hamilton population (-pCOHP) of NO_3^- adsorbed on a) $Cu_3Mo_2O_9/Cu^*$, b) $Cu^*_3Mo_2O_9/Cu$ and c) $Cu_3Mo^*_2O_9/Cu$ (the NO_3^- adsorption sites are indicated in red and marked with "*").

We explicitly calculated the cleavage energies of the low-index $Cu_3Mo_2O_9$ surfaces and found that the (002) termination showed the lowest surface energy among the tested planes. Thus, $Cu_3Mo_2O_9$ (002) is the most stable and representative surface under reaction conditions.

Table S1. Surface energy of $Cu_3Mo_2O_9$.

$Cu_3Mo_2O_9$	bulk	slab	E(eV/Å^2)	
020	-825.8274	-834.5279	-0.041308	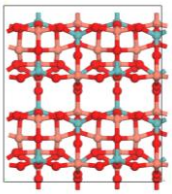
200	-1071.403	-1099.859	-0.141623	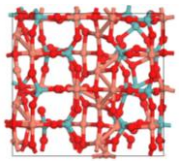
002	-736.27	-772.1355	-0.160227	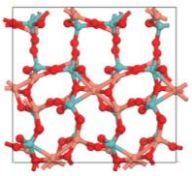

Table S2. NO_3^-RR performance, comparison with the state-of-the-art catalysts.

Catalyst	Electrolyte	FE[a]	YR[b]	YR[c]	Ref.
$Cu_3Mo_2O_9$/Cu	1 M KOH /0.05 M KNO_3	97.5% (-0.5 V_{RHE})	14.0 (-0.5 V_{RHE}) 19.3 (-0.7 V_{RHE})	19.3	This work
RuCu DAs/NGA	0.1 M KOH /0.1 M KNO_3	95.7% (-0.3 V_{RHE})	-	3.1	1
Fe_1/NC-900	0.1 M K_2SO_4/0.5 M KNO_3	86% (-0.7 V_{RHE})	18.8 (-0.9 V_{RHE})	-	3
Fe SAC	0.1 M K_2SO_4/0.5 M KNO_3	75% (-0.66 V_{RHE})	5.2	-	8
Co_3CuN	0.5 M KOH with 2000 ppm NO_3^-	97% (-0.3 V_{RHE})	7.8 (-0.6 V_{RHE})	-	9
O-Cu-PTCDA	0.1 M PBS with 500 ppm NO_3^-	85.9% (-0.4 V_{RHE})	-	0.5	10
$Cu_{50}Ni_{50}$	0.01 M KOH/0.5 M Na_2SO_4 /0.1 M NO_3^-	88% (-1.0 V_{RHE})	-	9.9	11
Co_1-P/NPG	0.5 M K_2SO_4/0.1 M KNO_3	93.8% (-0.7 V_{RHE})	21.7 (-0.9 V_{RHE})	-	16
Fe/Ni_2P	0.2 M K_2SO_4/50 mM NO_3^-	82.1% (-0.4 V_{RHE})	-	0.2	57
Fe_2TiO_5	PBS with 0.1 M $NaNO_3$	87.6% (-1.0 V_{RHE})	12.4	-	58
MP-Cu	1 M KOH /0.05 M NO_3^-	99.8% (-0.3 V_{RHE})	-	9.2 (-0.5 V_{RHE})	60
$ZnCo_2O_4$ NSA/CC	0.1 M NaOH/0.1 M $NaNO_3$	98.3% (-0.6 V_{RHE})	-	10.8 (-0.8 V_{RHE})	63
CeO_{2-x}@NC/GP	0.1 M NaOH/0.1 M NO_3^-	92.9% (-0.5 V_{RHE})	-	12.1 (-0.8 V_{RHE})	64
CoO/CuO-NA/CF	0.5 M NaOH with 250 ppm NO_3^-	92.9% (-0.2 V_{RHE})	-	5.0	65

[a]FE_{NH_3} (%). [b]YR_{NH_3} (mg_{NH_3} h^{-1} mg_{cat}^{-1}). [c]YR_{NH_3} (mg_{NH_3} $h^{-1}cm^{-2}$).